Tian Huang
Pujun Bai
Jiangping Mei[1]
e-mail: ppm@tju.edu.cn

Key Laboratory of Mechanism Theory and Equipment Design of State Ministry of Education,
Tianjin University,
Tianjin 300072, China

Derek G. Chetwynd
School of Engineering,
The University of Warwick,
Coventry CV4 7AL, UK

Tolerance Design and Kinematic Calibration of a 4-DOF Pick-and-place Parallel Robot

This paper presents a comprehensive methodology for ensuring the geometric pose accuracy of a 4-DOF high-speed pick-and-place parallel robot having an articulated travelling plate. The process is implemented by four steps: (1) formulation of the error model containing all possible geometric source errors; (2) tolerance design of the source errors affecting the uncompensatable pose accuracy via sensitivity analysis; (3) identification of the source errors affecting the compensatable pose accuracy via a simplified model and distance measurements; and (4) development of a linearized error compensator for real-time implementation. Experimental results show that a tilt angular accuracy of 0.1/100, and a volumetric/rotational accuracy of 0.5 mm/±0.8 deg of the end-effector can be achieved over the cylindrical task workspace.

1. Introduction

Four-DOF high-speed pick-and-place parallel robots using four identical R-$(SS)^2$ limbs linked to an articulated traveling plate have recently attracted great interest in academia and industry [1,2]. Here, R denotes an actuated revolute joint and $(SS)^2$ two spherical joints at either extremity of a spatial parallelogram.

As with other lower mobility robotic systems, the geometric pose accuracy of these devices is an important performance specification. It can be improved by kinematic calibration [3-11] provided that the uncompensatable pose error (the tilt angular error) of the end-effector can be effectively restrained *via* tolerance design, manufacturing and assembly. For example, the uncompensatable tilt angular error is mainly caused by imperfectness of spatial parallelograms, the relevant source errors must be strictly controlled prior to kinematic calibration [9-13].Generally, this requires that: (1) the error model be formulated in such a way that the source errors affecting the compensatable and uncompensatable pose accuracy can be separated in an explicit manner; (2) the uncompensatable pose error be held below an acceptable level over the workspace with feasible manufacturing cost such that it can reasonably be treated as the 'measurement noise' of a simplified error model for kinematic calibration; and (3) the source errors affecting the compensatable pose accuracy (three translations and one rotation about the vertical axis) be accurately and effectively estimated such that the inverse kinematic model residing in the controller more closely matches the real system. The both measures constitute the framework to ensure geometric pose accuracy of the end-effector. Figure 1 depicts a general roadmap helpful to understanding the problem to be investigated.

In the past decades, intensive studies have been carried out towards geometric pose accuracy improvement for robotic mechanisms in general and for lower mobility parallel robots in particular by tolerance design and kinematic calibration. The most commonly used methods to deal with tolerance allocation usually involves solving an optimization problem by minimizing

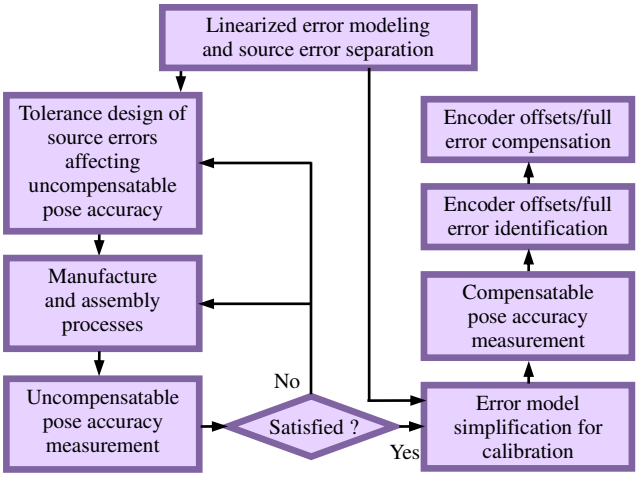

Fig.1 Roadmap for ensuring the geometric pose accuracy of the lower mobility robotic systems

manufacturing cost subject to the constraints represented by the specified allowable pose accuracy, the manufacturing feasibilities, etc. Building upon statistical or worst case error models, various cost-tolerance functions have been proposed for minimization, and several algorithms have been developed for improving computational efficiency [14-19]. The kernel step in kinematic calibration is to identify all the source errors affecting the compensatable pose accuracy using a full/partial set of error data which can be easily measured in a time and cost effective manner without compromising the accuracy of the end results. For the Delta-type parallel robots containing parallelograms, the external calibration is appropriate due to their topological structures in nature, and both coordinate and distance/1-dimensional based approaches can be adopted [7-9,11]. Compared with the coordinate based approach, the distance based approach is invariant with the reference frame chosen and needlessness to identify the rigid body motion with respect to the world frame since robot localization can be made afterwards according to the environment context. In addition, the conditions of identifiability has been proposed, and various observability indices have been developed for minimizing the number of

[1] Corresponding author

measurements without affecting identification accuracy [20-23].

Although a number of efforts have been made towards various aspects in error modeling, tolerance design and kinematic calibration of the Delta-type parallel robots [3, 7-9,11-14], a comprehensive methodology is still required to merge all threads into a framework. Therefore, addressing Fig.1 and taking such a 4-DOF parallel robot as an example, this paper proposes a systematic approach to improve the geometrical pose accuracy of the robot by integrating tolerance design with kinematic calibration. The remainder of this paper is organized as follows. In Section 2, a linearized error model containing all possible geometric source errors is formulated using the first order approximation, allowing the source errors affecting the compensatable and uncompensatable pose accuracy to be separated in an explicit manner. In Section 3, a statistical error model of the robot is formulated, leading to an optimal tolerance allocation by a very simple algorithm built upon sensitivity analysis. In Section 4, parameter identification is carried out using a simplified error model and distance measurements. The criterion to minimize the measurements is discussed and a linear compensator is designed for the real-time error compensation. In Section 5, experiments on a prototype machine are carried out to verify the effectiveness of the entire processes proposed before conclusions are drawn in Section 6.

2. Error Modelling

Figure 2(a) shows a 3D view of the proposed 4-DOF parallel robot [2]. It has two identical closed-loop sub-chains, each comprising two identical R-(SS)^2 limbs connected between the base at one end and either subpart 1 or 2 of the travelling plate at the other. Subparts 1 and 2 are articulated by ball-bearing guideways to subpart 3 as shown in Fig.2(b). The required rotation about the z axis is then generated from relative translation between subparts 1 and 2 *via* a rack-and-pinion assembly centred on subpart 3.

In order to formulate the error model containing all possible geometric source errors, the following points and frames are defined as shown in Fig.2(c) where the nominal dimensions of the links and the unit vectors of the frames are also depicted.

$C_{j,i}$ ($A_{j,i}$): The central point of the jth (j=1,2) S-joint on the proximal link(or on subpart 1 or 2) with C_i (A_i)being the middle point of $\overrightarrow{C_{1,i}C_{2,i}}$ ($\overrightarrow{A_{1,i}A_{2,i}}$);

B_i : The projection of C_i onto the rotatory axis of the R-joint;

$\{O\}$ ($\{O'\}$): The global reference (body fixed) frame attached to the base (or subpart 3);

$\left\{{}^0_0B_i\right\}$ ($\left\{{}^1_0B_i\right\}$): The local reference (body fixed) frame attached to the base (or the proximal link);

$\left\{{}^2_1C_i\right\}$ ($\left\{{}^3_{0'}A_i\right\}$): The body fixed frame of the S-joints attached to the proximal link (or subpart 1 or 2).

As shown in Fig.2(c), the jth loop closure equation within the ith limb can be expressed as

$$\begin{aligned}\boldsymbol{r} = \boldsymbol{b}_i + L_i\boldsymbol{R}_{0,i}\boldsymbol{R}_{1,i}\boldsymbol{e}_1 + \frac{1}{2}\mathrm{sgn}(j)c_{c,i}\boldsymbol{R}_{0,i}\boldsymbol{R}_{1,i}\boldsymbol{R}_{2,i}\boldsymbol{e}_3 + l_{j,i}\hat{\boldsymbol{l}}_{j,i} \\ -\frac{1}{2}\mathrm{sgn}(j)c_{a,i}\boldsymbol{R}\boldsymbol{R}_{3,i}\boldsymbol{e}_3 - \boldsymbol{R}\left(\boldsymbol{a}_i + \mu_i s\hat{\boldsymbol{s}}\right)\end{aligned} \tag{1}$$

$$\boldsymbol{R}_{0,i} = \mathrm{Rot}\left(z,\gamma_i\right)\mathrm{Rot}\left(x_{0,i},\frac{\pi}{2}+\Delta\alpha_{0,i}\right)\mathrm{Rot}\left(y_{0,i},\Delta\beta_{0,i}\right)$$

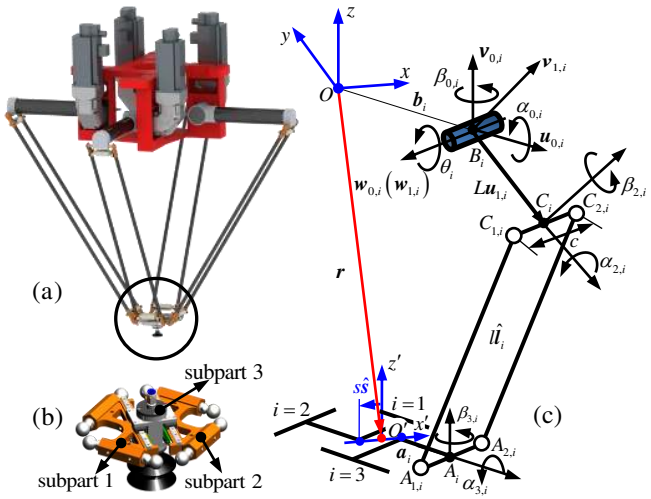

Fig.2 A CAD model and kinematic diagram of the parallel robot with articulated traveling plate

$$\boldsymbol{R}_{1,i}=\mathrm{Rot}\left(z_{1,i},\theta_i+\Delta\theta_i\right),\ \boldsymbol{R}_{2,i}=\mathrm{Rot}\left(x_{1,i},\Delta\alpha_{2,i}\right)\mathrm{Rot}\left(y_{2,i},\Delta\beta_{2,i}\right)$$

$$\boldsymbol{R}_{3,i} = \mathrm{Rot}\left(z',\gamma_i\right)\mathrm{Rot}\left(x_{3,i},\frac{\pi}{2}+\Delta\alpha_{3,i}\right)\mathrm{Rot}\left(y_{3,i},\Delta\beta_{3,i}\right)$$

$$\boldsymbol{R} = \mathrm{Rot}\left(x,\Delta\alpha\right)\mathrm{Rot}\left(y,\Delta\beta\right)\mathrm{Rot}\left(z,\Delta\gamma\right)$$

$$\boldsymbol{e}_1=\begin{pmatrix}1 & 0 & 0\end{pmatrix}^{\mathrm{T}},\boldsymbol{e}_3=\begin{pmatrix}0 & 0 & 1\end{pmatrix}^{\mathrm{T}}$$

$$\mathrm{sgn}(j)=\begin{cases}1 & j=1\\ -1 & j=2\end{cases},\ \mu_i=\begin{cases}1 & i=1,2\\ -1 & i=3,4\end{cases},\ \gamma_i=-\frac{\pi}{4}+\frac{\pi}{2}(i-1)$$

where

$\boldsymbol{R}_{0,i}$: The rotation matrix of $\left\{{}^0_0B_i\right\}$ with respect to $\{O\}$

$\boldsymbol{R}_{1,i}$: The rotation matrix of $\left\{{}^1_0B_i\right\}$ with respect to $\left\{{}^0_0B_i\right\}$

$\boldsymbol{R}_{2,i}$: The rotation matrix of $\left\{{}^2_1C_i\right\}$ with respect to $\left\{{}^1_0B_i\right\}$

$\boldsymbol{R}_{3,i}$: The rotation matrix of $\left\{{}^3_{0'}A_i\right\}$ with respect to $\{O'\}$

$\boldsymbol{R}$: The rotation matrix of $\{O'\}$ with respect to $\{O\}$

$L_i = L+\Delta L_i$, $l_{j,i} = l+\Delta l_{j,i}$, $c_{c,i} = c+\Delta c_{c,i}$ ($c_{a,i} = c+\Delta c_{a,i}$) : The actual and nominal lengths of $\overrightarrow{B_iC_i}$, $\overrightarrow{C_iA_i}$, $\overrightarrow{C_{1,i}C_{2,i}}$ ($\overrightarrow{A_{1,i}A_{2,i}}$) and their errors

$\boldsymbol{r}=\boldsymbol{r}_0+\Delta\boldsymbol{r}$: The actual, nominal and error vectors of O' evaluated in $\{O\}$

$\hat{\boldsymbol{l}}_{j,i}=\hat{\boldsymbol{l}}_i+\Delta\hat{\boldsymbol{l}}_{j,i}$: The unit actual, nominal and error vectors of $\overrightarrow{C_{j,i}A_{j,i}}$ evaluated in $\{O\}$

$\boldsymbol{a}_i=\boldsymbol{a}_{0i}+\Delta\boldsymbol{a}_i$: The actual, nominal and error vectors of A_i evaluated in $\{O'\}$

$\boldsymbol{b}_i=\boldsymbol{b}_{0i}+\Delta\boldsymbol{b}_i$: The actual, nominal and error vectors of B_i evaluated in $\{O\}$

$\hat{\boldsymbol{s}}=\hat{\boldsymbol{s}}_0+\Delta\hat{\boldsymbol{s}}$: The unit actual, nominal and error vectors of sliding direction of part 3 relative to part 1(2) evaluated in $\{O'\}$

$s=s_0+\Delta s$: The actual, nominal and error sliding distance of part 3 relative to part 1(2)

θ_i , $\Delta\theta_i$: The nominal angular and encoder offset of $\overrightarrow{B_iC_i}$

$\Delta\alpha_{0,i}, \Delta\beta_{0,i}$; $\Delta\alpha_{2,i}, \Delta\beta_{2,i}$; $\Delta\alpha_{3,i}, \Delta\beta_{3,i}$: The structural angular errors of $\{{}^0B_i\}$ relative to $\{O\}$; $\{{}^2_1C_i\}$ relative to $\{{}^1_0B_i\}$; and $\{{}^3_{0'}A_i\}$ relative to $\{O'\}$

$\Delta\alpha$, $\Delta\beta$, $\Delta\gamma$: The angular errors of $\{O'\}$ relative to $\{O\}$

Adding and subtracting two loop closure equations associated with the *i*th limb, leads to

$$\boldsymbol{r} = \boldsymbol{b}_i + L_i\boldsymbol{R}_{0,i}\boldsymbol{R}_{1,i}\boldsymbol{e}_1 + \frac{l_{1,i}\hat{\boldsymbol{l}}_{1,i} + l_{2,i}\hat{\boldsymbol{l}}_{2,i}}{2} - \boldsymbol{R}\left(\boldsymbol{a}_i + \mu_i s\hat{\boldsymbol{s}}\right) \tag{2a}$$

$$c_{c,i}\boldsymbol{R}_{0,i}\boldsymbol{R}_{1,i}\boldsymbol{R}_{2,i}\boldsymbol{e}_3 - c_{a,i}\boldsymbol{R}\boldsymbol{R}_{3,i}\boldsymbol{e}_3 + l_{1,i}\hat{\boldsymbol{l}}_{1,i} - l_{2,i}\hat{\boldsymbol{l}}_{2,i} = 0 \tag{2b}$$

Since the source errors normally are very small compared to their nominal values, it is reasonable to use a linearized error model for tolerance design of geometric source errors. Then, rough kinematic calibration is required to reduce the encoder offsets in an iterative manner until the linearized error model is valid for fine kinematic calibration. This issue will be discussed in Section 5. Thus, the first order approximation of Eqs.(2a) and (2b) can be made such that

$$\begin{aligned}
&\Delta\boldsymbol{r} + \boldsymbol{\varepsilon}\times\boldsymbol{a}_{s,i} + \mu_i\Delta s\hat{\boldsymbol{s}}_0 = \\
&\Delta\boldsymbol{e}_i + \Delta L_i\boldsymbol{u}_{1,i} + \Delta\bar{l}_i\hat{\boldsymbol{l}}_i + \bar{l}\bar{\boldsymbol{\varepsilon}}_i\times\hat{\boldsymbol{l}}_i \qquad (3a)\\
&+L\left(\Delta\alpha_{0,i}\sin\theta_i\boldsymbol{w}_{0,i} - \Delta\beta_{0,i}\cos\theta_i\boldsymbol{w}_{0,i} + \Delta\theta_i\boldsymbol{v}_{1,i}\right)\\
&\boldsymbol{\varepsilon}\times\boldsymbol{w}_{0,i} = \\
&-\Delta\alpha_{03,i}\boldsymbol{v}_{0,i} + \Delta\beta_{03,i}\boldsymbol{u}_{0,i} - \Delta\alpha_{2,i}\boldsymbol{v}_{1,i} + \Delta\beta_{2,i}\boldsymbol{u}_{1,i} \qquad (3b)\\
&+\frac{\Delta\tilde{c}_i}{c}\boldsymbol{w}_{0,i} + \frac{\Delta\tilde{l}_i}{c}\hat{\boldsymbol{l}}_i + \frac{l}{c}\tilde{\boldsymbol{\varepsilon}}_i\times\hat{\boldsymbol{l}}_i
\end{aligned}$$

$$\Delta\bar{l}_i = \frac{\Delta l_{1,i} + \Delta l_{2,i}}{2}\ ,\ \bar{\boldsymbol{\varepsilon}}_i = \frac{\boldsymbol{\varepsilon}_{1,i} + \boldsymbol{\varepsilon}_{2,i}}{2}$$

$$\Delta\tilde{l}_i = \Delta l_{1,i} - \Delta l_{2,i}\ ,\ \Delta\tilde{c}_i = \Delta c_{c,i} - \Delta c_{a,i}$$

$$\Delta\alpha_{03,i} = \Delta\alpha_{0,i} - \Delta\alpha_{3,i}\ ,\ \Delta\beta_{03,i} = \Delta\beta_{0,i} - \Delta\beta_{3,i}$$

$$\Delta\boldsymbol{e}_i = \Delta\boldsymbol{b}_i - \Delta\boldsymbol{a}_i\ ,\ \boldsymbol{a}_{s,i} = \boldsymbol{a}_{0i} + \mu_i s_0\hat{\boldsymbol{s}}_0$$

where

$\boldsymbol{\varepsilon}$, $\boldsymbol{\varepsilon}_{j,i}$: The angular error vectors of part 3 and $\overrightarrow{C_{j,i}A_{j,i}}$

$\boldsymbol{u}_{0,i}$, $\boldsymbol{v}_{0,i}$, $\boldsymbol{w}_{0,i}$ ($\boldsymbol{u}_{1,i}$, $\boldsymbol{v}_{1,i}$, $\boldsymbol{w}_{1,i}$): The nominal unit vectors of $\{{}^0B_i\}$ ($\{{}^1_0B_i\}$)

Taking the dot products on both sides of Eqs.(3a) and (3b) with $\hat{\boldsymbol{l}}_i$, and rewriting in matrix form, yields

$$\begin{bmatrix}\boldsymbol{A}_{\delta\delta} & \boldsymbol{A}_{\delta\varepsilon}\\ \boldsymbol{0} & \boldsymbol{A}_{\varepsilon\varepsilon}\end{bmatrix}\begin{pmatrix}\boldsymbol{\delta}\\ \boldsymbol{\varepsilon}\end{pmatrix} = \begin{bmatrix}\boldsymbol{B}_\delta & \boldsymbol{0}\\ \boldsymbol{0} & \boldsymbol{B}_\varepsilon\end{bmatrix}\begin{pmatrix}\Delta\boldsymbol{p}_\delta\\ \Delta\boldsymbol{p}_\varepsilon\end{pmatrix} \tag{4}$$

where

$$\boldsymbol{\delta} = (\Delta\boldsymbol{r}^{\mathrm{T}} \quad \Delta s)^{\mathrm{T}}\ ,\ \boldsymbol{A}_{\delta\delta} = \begin{bmatrix}\hat{\boldsymbol{l}}_1 & \cdots & \hat{\boldsymbol{l}}_4\\ \mu_1\hat{\boldsymbol{l}}_1^{\mathrm{T}}\hat{\boldsymbol{s}} & \cdots & \mu_4\hat{\boldsymbol{l}}_4^{\mathrm{T}}\hat{\boldsymbol{s}}\end{bmatrix}^{\mathrm{T}}$$

$$\boldsymbol{A}_{\delta\varepsilon} = \begin{bmatrix}\boldsymbol{a}_{s,1}\times\hat{\boldsymbol{l}}_1 & \cdots & \boldsymbol{a}_{s,4}\times\hat{\boldsymbol{l}}_4\end{bmatrix}^{\mathrm{T}},\ \boldsymbol{A}_{\varepsilon\varepsilon} = \begin{bmatrix}\boldsymbol{w}_{0,1}\times\hat{\boldsymbol{l}}_1 & \cdots & \boldsymbol{w}_{0,4}\times\hat{\boldsymbol{l}}_4\end{bmatrix}^{\mathrm{T}}$$

$$\boldsymbol{B}_\delta = \mathrm{diag}\left[\boldsymbol{B}_{\delta,i}\right],\ \boldsymbol{B}_\varepsilon = \mathrm{diag}\left[\boldsymbol{B}_{\varepsilon,i}\right]$$

$$\boldsymbol{B}_{\delta,i} = \begin{bmatrix}\hat{\boldsymbol{l}}_i^{\mathrm{T}}\boldsymbol{v}_{1,i} & \hat{\boldsymbol{l}}_i^{\mathrm{T}} & \hat{\boldsymbol{l}}_i^{\mathrm{T}}\boldsymbol{u}_{1,i} & \sin\theta_i\hat{\boldsymbol{l}}_i^{\mathrm{T}}\boldsymbol{w}_{0,i} & -\cos\theta_i\hat{\boldsymbol{l}}_i^{\mathrm{T}}\boldsymbol{w}_{0,i} & 1\end{bmatrix}$$

$$\boldsymbol{B}_{\varepsilon,i} = \begin{bmatrix}1 & \hat{\boldsymbol{l}}_i^{\mathrm{T}}\boldsymbol{w}_{0,i} & -\hat{\boldsymbol{l}}_i^{\mathrm{T}}\boldsymbol{v}_{0,i} & \hat{\boldsymbol{l}}_i^{\mathrm{T}}\boldsymbol{u}_{0,i} & -\hat{\boldsymbol{l}}_i^{\mathrm{T}}\boldsymbol{v}_{1,i} & \hat{\boldsymbol{l}}_i^{\mathrm{T}}\boldsymbol{u}_{1,i}\end{bmatrix}$$

$$\Delta\boldsymbol{p}_\delta = (\Delta\boldsymbol{p}_{\delta,1}^{\mathrm{T}} \quad \cdots \quad \Delta\boldsymbol{p}_{\delta,4}^{\mathrm{T}})^{\mathrm{T}},\ \Delta\boldsymbol{p}_\varepsilon = (\Delta\boldsymbol{p}_{\varepsilon,1}^{\mathrm{T}} \quad \cdots \quad \Delta\boldsymbol{p}_{\varepsilon,4}^{\mathrm{T}})^{\mathrm{T}}$$

$$\Delta\boldsymbol{p}_{\delta,i} = (L\Delta\theta_i \quad \Delta\boldsymbol{e}_i^{\mathrm{T}} \quad \Delta L_i \quad L\Delta\alpha_{0,i} \quad L\Delta\beta_{0,i} \quad \Delta\bar{l}_i)^{\mathrm{T}}$$

$$\Delta\boldsymbol{p}_{\varepsilon,i} = (\Delta\tilde{l}_i/c \quad \Delta\tilde{c}_i/c \quad \Delta\alpha_{03,i} \quad \Delta\beta_{03,i} \quad \Delta\alpha_{2,i} \quad \Delta\beta_{2,i})^{\mathrm{T}}$$

Assuming that $\boldsymbol{A}_{\delta\delta}$ and $\boldsymbol{A}_{\varepsilon\varepsilon}^{\mathrm{T}}\boldsymbol{A}_{\varepsilon\varepsilon}$ are non-singular finally results in

$$\boldsymbol{\delta} = \boldsymbol{G}_{\delta\delta}\Delta\boldsymbol{p}_\delta + \boldsymbol{G}_{\delta\varepsilon}\Delta\boldsymbol{p}_\varepsilon \tag{5}$$

$$\boldsymbol{\varepsilon} = \boldsymbol{G}_{\varepsilon\varepsilon}\Delta\boldsymbol{p}_\varepsilon \tag{6}$$

$$\boldsymbol{G}_{\delta\delta} = \boldsymbol{A}_{\delta\delta}^{-1}\boldsymbol{B}_\delta,\ \boldsymbol{G}_{\delta\varepsilon} = -\boldsymbol{A}_{\delta\delta}^{-1}\boldsymbol{A}_{\delta\varepsilon}\boldsymbol{A}_{\varepsilon\varepsilon}^{+}\boldsymbol{B}_\varepsilon,\ \boldsymbol{G}_{\varepsilon\varepsilon} = \boldsymbol{A}_{\varepsilon\varepsilon}^{+}\boldsymbol{B}_\varepsilon$$

Here, $\boldsymbol{A}_{\varepsilon\varepsilon}^{+}$ denotes the pseudo-inverse of $\boldsymbol{A}_{\varepsilon\varepsilon}$ due to the over-constraint imposed by the limbs onto the travelling plate.

Eqs. (5) and (6) show that the source errors of the robot can be divided into two groups, $\Delta\boldsymbol{p}_\delta$ and $\Delta\boldsymbol{p}_\varepsilon$ .The first contains 32 source errors affecting the positioning accuracy of O' and the rotational accuracy about the *z* axis of the end-effector relative to subpart 3 if it is assumed to undergo pure translation. The second contains 24 source errors affecting the angular accuracy of subpart 3.

It is easy to see that $\boldsymbol{\delta}$ is compensatable because a linear error compensator $\Delta\boldsymbol{q}_m = L\left(\Delta\theta_{m,1} \quad \cdots \quad \Delta\theta_{m,4}\right)^{\mathrm{T}}$ can be designed that enables the nominal angular displacements of the actuated joints to be modified such that

$$\boldsymbol{\delta} = \boldsymbol{G}_{\delta\delta}\Delta\boldsymbol{p}_\delta + \boldsymbol{G}_{\delta\varepsilon}\Delta\boldsymbol{p}_\varepsilon + \boldsymbol{A}_{\delta\delta}^{-1}\boldsymbol{B}_m\Delta\boldsymbol{q}_m \to \boldsymbol{0}\ ,\ \boldsymbol{B}_m = \mathrm{diag}\left[\hat{\boldsymbol{l}}_i^{\mathrm{T}}\boldsymbol{v}_{1,i}\right] \tag{7a}$$

or

$$\boldsymbol{B}_\delta\Delta\boldsymbol{p}_\delta - \boldsymbol{A}_{\delta\varepsilon}\boldsymbol{A}_{\varepsilon\varepsilon}^{+}\boldsymbol{B}_\varepsilon\Delta\boldsymbol{p}_\varepsilon + \boldsymbol{B}_m\Delta\boldsymbol{q}_m \to \boldsymbol{0} \tag{7b}$$

It can be seen from Eq.(7b) that $\Delta\boldsymbol{q}_m$ can be determined by

$$\Delta\boldsymbol{q}_m = -\boldsymbol{B}_m^{-1}\left(\boldsymbol{B}_\delta\Delta\boldsymbol{p}_\delta - \boldsymbol{A}_{\delta\varepsilon}\boldsymbol{A}_{\varepsilon\varepsilon}^{+}\boldsymbol{B}_\varepsilon\Delta\boldsymbol{p}_\varepsilon\right) \tag{8}$$

as long as $\Delta\boldsymbol{p}_\delta$ and $\Delta\boldsymbol{p}_\varepsilon$ are estimated via parameter identification. However, examining Eq.(6) shows that $\boldsymbol{\varepsilon}$ is free of reference frame chosen, uncompensatable and has significant bearing on $\boldsymbol{\delta}$ due to the existence of $\Delta\boldsymbol{p}_\varepsilon$ as shown in Eq.(5). Thus, $\boldsymbol{\varepsilon}$ must be restrained below a specified level by mechanical measures such that the kinematic calibration can be carried out using a simplified kinematic model valid only when the angular error caused by $\Delta\boldsymbol{p}_\varepsilon$ is sufficiently small. This goal can be achieved by tolerance design of $\Delta\boldsymbol{p}_\varepsilon$ as addressed in what follows.

3. Tolerance Design

3.1 Probability model

There are two main strategies in error analysis and tolerance design of robotic systems, i.e. the worst case method and the statistical method. For the sake of using group technology in assembly processes of four identical limbs, the statistic method is used here. In order to facilitate tolerance design, a probability model is required since $\Delta\boldsymbol{p}_\varepsilon$ is random in nature. So, rewrite Eq.(6) as

$$\boldsymbol{\varepsilon} = \sum_{i=1}^{4}\boldsymbol{G}_{\varepsilon\varepsilon,i}\Delta\boldsymbol{p}_{\varepsilon,i}\ ,\ \boldsymbol{\varepsilon} = (\varepsilon_x \quad \varepsilon_y \quad \varepsilon_z)^{\mathrm{T}} \tag{9}$$

Here, only the tilt angular error $\varepsilon_\theta = \sqrt{\varepsilon_x^2 + \varepsilon_y^2}$ is considered

because it heavily affects the positioning accuracy of subpart 3. Assume that the source errors are independent and zero mean, and that components of the same type have equal variances as the robot has four identical limbs, i.e.

$$\sigma(\Delta p_{\varepsilon,k}) = \sigma(\Delta p_{\varepsilon,i,k}),\ i=1,2,3,4 \tag{10}$$

where $\Delta p_{\varepsilon,i,k}$ denotes the kth component in $\Delta \boldsymbol{p}_{\varepsilon,i}$. Then,

$$\Delta p_{\varepsilon,1} = \Delta\tilde{l}/c,\ \Delta p_{\varepsilon,2} = \Delta\tilde{c}/c,\ \Delta p_{\varepsilon,3} = \Delta\alpha_{03}$$
$$\Delta p_{\varepsilon,4} = \Delta\beta_{03},\ \Delta p_{\varepsilon,5} = \Delta\alpha_2,\quad \Delta p_{\varepsilon,6} = \Delta\beta_2$$

Thus, the probability model of ε_θ *vs.* all $\Delta p_{\varepsilon,k}$ can be formulated as

$$\sigma^2(\varepsilon_\theta) = \sum_{k=1}^{6} \mu_{\theta,k}^2 \sigma^2(\Delta p_{\varepsilon,k}),\ \mu_{\theta,k} = \sqrt{\sum_{i=1}^{4}(g_{i,1,k}^2 + g_{i,2,k}^2)} \tag{11}$$

where $\mu_{\theta,k}$ is defined as the local sensitivity of $\sigma(\varepsilon_\theta)$ with regard to $\Delta p_{\varepsilon,k}$ and $g_{i,j,k}$ is the element of the jth row and the kth column of $\boldsymbol{G}_{\varepsilon\varepsilon,i}$ .Furthermore, the mean value of $\mu_{\theta,k}$, i.e. $\bar{\mu}_{\theta,k} = \left(\int_V \mu_{\theta,k} dV\right) \Big/ V$, over the entire task workspace, is defined as the global sensitivity [10], which can then be used as an index to evaluate the impact of $\Delta p_{\varepsilon,k}$ on ε_θ in a global sense.

3.2 Optimal tolerance allocation

Generally, manufacturing cost and tilt angular accuracy are two conflicting criteria for optimal tolerance design of the source errors and several cost-tolerance functions have been proposed [24]. The simplest way to formulate the function is to assume that the cost is inversely proportional to the relevant tolerance. Therefore, the problem of optimal tolerance allocation can be stated as: Minimize the total cost while satisfying the constraints imposed upon: (i) the maximum allowable tilt angular error over the task workspace, and (ii) the lower bounds of the source errors due to manufacturing feasibility. Meanwhile, if the global sensitivities are considered as the indices reflecting the degrees of importance such that $\bar{\mu}_k \sigma(\Delta p_{\varepsilon,k}) = \text{const}$,the constrained nonlinear programming problem can be formulated as

$$f = \sum_{k=1}^{6} w_k \sigma^{-1}(\Delta p_{\varepsilon,k}) \to \min \tag{12}$$

$$\text{s.t.} \begin{cases} \sum_{k=1}^{6} w_k = 1,\quad 0 \le w_k \le 1 \\ \max_{x \in W_t}\left(\sigma(\varepsilon_\theta)\right) - \sigma_\theta^U \le 0 \\ \sigma(\Delta p_{\varepsilon,k}) - \dfrac{\max(\bar{\mu}_{\theta,k})}{\bar{\mu}_{\theta,k}} \sigma(\Delta p_{\varepsilon,\text{ref}}) = 0 \\ \sigma(\Delta p_{\varepsilon,\text{ref}}) \ge \sigma_{\varepsilon,\text{ref}}^L \end{cases}$$

where σ_θ^U is the upper bound of the standard deviation of ε_θ; $\sigma(\Delta p_{\varepsilon,\text{ref}}) = \min\left(\sigma(\Delta p_{\varepsilon,k})\right)$ is defined as the reference level of all standard deviations; $\sigma_{\varepsilon,\text{ref}}^L$ is the lower bound of $\sigma(\Delta p_{\varepsilon,\text{ref}})$; w_k is the normalized weight of manufacturing cost associated with the kth standard deviation. This formulation has the merit that it involves only one design variable, $\sigma(\Delta p_{\varepsilon,\text{ref}})$, allowing the problem to be efficiently solved by a 1-D root searching algorithm. Then, the tolerance of $\Delta p_{\varepsilon,k}$ can be calculated according to 3σ criterion.

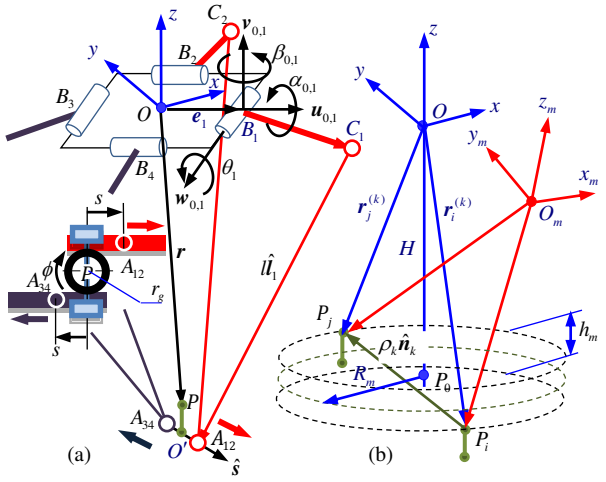

Fig.3 A simplified model for kinematic calibration

$$T_{\varepsilon,k} = \pm 3\sigma(\Delta p_{\varepsilon,k}) \tag{13}$$

4. Identification and Compensation

Once a combination of tolerance design, manufacturing and assembly processes ensures that ε_θ is held below an acceptable level such that $|\boldsymbol{G}_{\delta\varepsilon}\Delta\boldsymbol{p}_\varepsilon|$ in Eq.(5) becomes much smaller than $|\boldsymbol{G}_{\delta\delta}\Delta\boldsymbol{p}_\delta|$ over the task workspace, a simplified model can be created as shown in Fig.3(a). In this sense, $\Delta\boldsymbol{p}_\varepsilon$ can be treated as the unmodeled error and thus $\boldsymbol{G}_{\delta\varepsilon}\Delta\boldsymbol{p}_\varepsilon$ as the 'measurement noise'. So, Eq.(5) simplifies to

$$\boldsymbol{\delta} \approx \boldsymbol{G}_{\delta\delta}\Delta\boldsymbol{p}_\delta \tag{14}$$

4.1 Identification model using distance measurement

Building upon the simplified error model represented by Eq.(14), namely subparts 1 and 2 undergo pure translation, the distance based approach is employed for the identification of $\Delta\boldsymbol{p}_\delta$ by using a set of distance measurements either directly achieved by a metrology device, a DBB system [6] for example, or extracted from other measurements, such as a laser tracker [7] or dedicated artefacts [8]. The advantages of the distance based approach lies in that it is invariant with the reference frame choice and it is unnecessary to identify the source errors describing the rigid body motion of robot frame relative to the world frame since robot localization can be made afterwards according to the environment context.

As shown in Fig.3(b), the position vector of P on subpart 3 with regard to a metrology frame $\{O_m\}$ decomposes into two components, i.e. the position vector of P relative to $\{O\}$ and that of O relative to $\{O_m\}$. Because the distance between two positions of P is invariant with the frame chosen, $\Delta\boldsymbol{p}_\delta$ can be identified using distance measurements as long as $\{O\}$ is specified by eliminating the rigid body motion of $\{O\}$ relative to.

For this reason, assume that (amongst many other possible choices) the following source errors in $\Delta\boldsymbol{p}_\delta$ vanish:

$$\Delta e_{x,2} = \Delta e_{z,2} = \Delta e_{z,3} = \Delta e_{x,4} = \Delta e_{y,4} = \Delta e_{z,4} = 0 \quad (15)$$

This treatment turns Eq.(14) into a model containing 26 source errors but it is convenient to keep it in the current form.

Drawing upon the argument that the source errors of parallel mechanisms can be identified using a partial set of measurement data as long as the source errors being identified are irreducible and the end-effector experiences its full degrees of freedom [25], two position vectors of P, P_i and P_j ($i \neq j$) are used to form a measurement pair numbered by k as shown in Fig.3(b), resulting in $K = C_N^2 = N(N-1)$ distance measurements that can be generated by the combinations of all the possible pairs of N poses. Thus, the corresponding loop closure equation can be expressed as

$$\rho_k \hat{\boldsymbol{n}}_k = \boldsymbol{r}_j^{(k)} - \boldsymbol{r}_i^{(k)}, \ k = 1, 2, \ldots, K \quad (16)$$

where ρ_k and $\hat{\boldsymbol{n}}_k$ denote the distance and unit vector of $\overrightarrow{P_i P_j}$.

Taking the first order approximation and the dot product on both sides of Eq.(16) with $\hat{\boldsymbol{n}}_k$, yields

$$\Delta\boldsymbol{\rho} = \boldsymbol{H}\Delta\boldsymbol{p}_\delta, \ \boldsymbol{H} = \begin{bmatrix} \boldsymbol{H}_1^{\mathrm{T}} & \cdots & \boldsymbol{H}_K^{\mathrm{T}} \end{bmatrix}, \ \boldsymbol{H}_k = \hat{\boldsymbol{n}}_k^{\mathrm{T}} \left(\boldsymbol{G}_{r,j} - \boldsymbol{G}_{r,i} \right) \quad (17)$$

where $\Delta\boldsymbol{\rho} = (\Delta\rho_1 \ \cdots \ \Delta\rho_K)^{\mathrm{T}}$, $\Delta\rho_k$ is the distance error of $\overrightarrow{P_i P_j}$; $\boldsymbol{G}_{r,i}$ and $\boldsymbol{G}_{r,j}$ are the partitioned matrices formed by the first three rows of $\boldsymbol{G}_{\delta\delta}$.

4.2 Optimal pose selection

In the implementation of kinematic calibration, choosing a set of optimal poses is an important issue to ensure the measurement efficiency and the identification accuracy.

4.2.1 Pose selection for fine identification

The straightforward and reasonable way to identify the full set of source errors is to take the central point P_0 of the cylindrical task workspace as the home position, and to choose n evenly spaced points on top (bottom) layer of the workspace boundary shown in Fig. 3(b). Meanwhile, let the nominal rotational angle $\phi_0 = s_0 / r_g$ of subpart 3 take the extreme value π ($-\pi$) when it travels on top (bottom) layer. This is because: (1) the necessary and sufficient condition for the full set of source errors to be identifiable requires the subpart 3 to experience all controllable degrees of freedom [25], i.e. three translations and one rotation in this case, and (2) the optimal poses tend to converge to the workspace boundary [26] where the highest signal/noise ratio can be achieved.

Five observability indices have been proposed for the optimal selection of calibration poses [27-29]. A comparison study shows that reciprocal of the condition number of the identification Jacobian, represented by O_2, is the most appropriate criterion. Thus, the pose selection problem can be stated as: To minimize n subject to the given threshold ε_0 defined as the relative change of $O_2^{(n)} = O_2\left(\boldsymbol{H}(n)\right) vs.\ n$, i.e.

$$\begin{aligned} &\min \ n \\ &\text{s.t.} \ \ \varepsilon = \frac{\left| O_2^{(n)} - O_2^{(n-1)} \right|}{O_2^{(n)}} \times 100\% \le \varepsilon_0 \\ &K = C_{2n+1}^2 \ge 26 \end{aligned} \quad (18)$$

Based upon the distance error model given by Eq.(17), full source errors, $\Delta\boldsymbol{p}_\delta$, can be estimated by the linear least square algorithm

$$\Delta\hat{\boldsymbol{p}}_\delta = \boldsymbol{H}^{+}\Delta\boldsymbol{\rho} \quad (19)$$

where $\boldsymbol{H}^{+} = \left(\boldsymbol{H}^{\mathrm{T}}\boldsymbol{H}\right)^{-1}\boldsymbol{H}^{\mathrm{T}}$ is the pseudo inverse of $\boldsymbol{H}$.

4.2.2 Pose selection for rough identification

Since the pose error caused by the encoder offsets is usually much larger than that caused by the others source errors, it is necessary to implement rough calibration first by only taking into account the encoder offsets such that these source errors are reduced below the level at which the linearized model is valid for full parameter identification and error compensation. Thus, the optimal pose selection problem for the rough calibration can be modified as

$$\begin{aligned} &\min \ n \\ &\text{s.t.} \ \ \varepsilon = \frac{\left| O_2^{(n)} - O_2^{(n-1)} \right|}{O_2^{(n)}} \times 100\% \le \varepsilon_0 \\ &K = C_{n+1}^2 \ge 4 \end{aligned} \quad (20)$$

where $n \ge 3$ denotes the number of evenly spaced points in a single layer, e.g. the middle layer shown in Fig.3 (b). Note that the nominal rotational angle ϕ can be kept unchanged, e.g. $\phi \equiv 0$ in the rough calibration. Hence, the encoder offsets $\Delta\boldsymbol{p}_\theta$ in the rough calibration can be estimated by

$$\Delta\hat{\boldsymbol{p}}_\theta = \boldsymbol{H}_\theta^{+}\Delta\boldsymbol{\rho}, \ \Delta\hat{\boldsymbol{p}}_\theta = L\left(\Delta\hat{\theta}_1 \quad \Delta\hat{\theta}_2 \quad \Delta\hat{\theta}_3 \quad \Delta\hat{\theta}_4\right)^{\mathrm{T}} \quad (21)$$

where $\boldsymbol{H}_\theta$ denotes the sub-matrix of $\boldsymbol{H}$, generated by the columns associated with $\Delta\boldsymbol{p}_\theta$

4.3 Linear error compensator

By assuming that the tilt angular error arising from $\Delta\boldsymbol{p}_\varepsilon$ has been restrained below an acceptable level such that it can be treated as 'measurement noise', the linear error compensator in Eq.(8) simplifies to
For rough calibration:

$$\Delta\boldsymbol{q}_m = -\Delta\hat{\boldsymbol{p}}_\theta \quad (22)$$

For fine calibration:

$$\Delta\boldsymbol{q}_m = -\boldsymbol{B}_m^{-1}\boldsymbol{B}_\delta\Delta\hat{\boldsymbol{p}}_\delta \quad (23)$$

Obviously, $\Delta\boldsymbol{q}_m$ is a function of the estimated source errors, the nominal dimensions and the configuration of the system. It is important to note that the encoder offsets have non-negligible bearings on the linearization of error modelling, therefore the rough calibration should be carried out in an iterative manner until the estimated parameters converge to a specified threshold such that linearized error model is valid for fine calibration.

5. Experiment Verifications

Tolerance design and kinematic calibration on a prototype of the 4-DOF parallel robot shown in Fig.4 are carried out to verify the effectiveness of the proposed methodology. Tested by ISO 9283-1998 [30], the positioning repeatability of subpart 3 is ±0.05mm and its rotational repeatability is ±0.3° over the cylindrical task workspace. The nominal dimensions of the links and the workspace are given in Table 1.

5.1 Verification of tolerance design

Figure 5 shows the global sensitivities of the sources errors affecting the uncompensatable pose accuracy of part 3. It is easy

Table 1 Nominal dimensions and the task workspace (mm)

b	a	L	l	c	R	H	h	r_g	s
200	75	375	950	100	500	763	250	12	$[-r_g\pi, r_g\pi]$

b, a --Radii of circumcircles of the base and traveling plate; R, h --Radius and height of the workspace; r_g --Radius of the pinion.

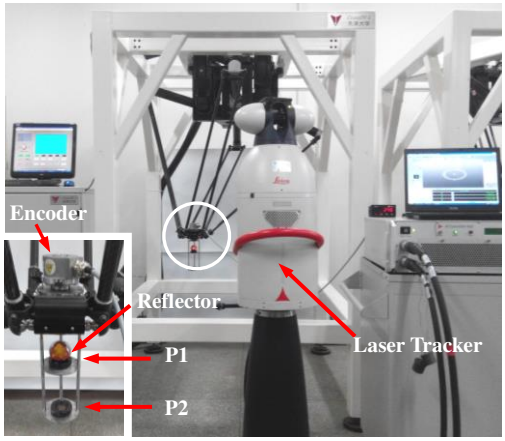

Fig.4 The experiment set-up

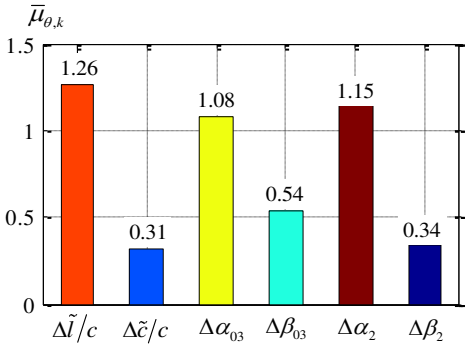

Fig.5 The global sensitivities of $\sigma(\varepsilon_\theta)$ *vs.* $\sigma(\Delta p_{\varepsilon,k})$.

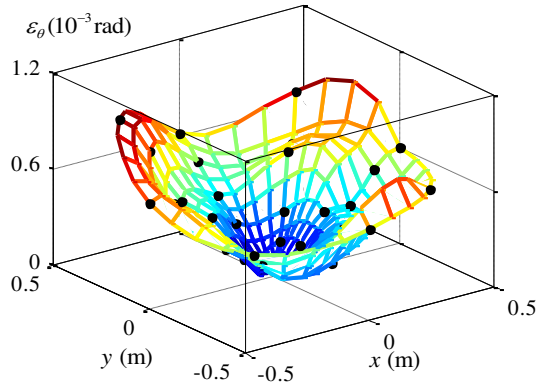

Fig.6 Distributions of ε_θ in the bottom layer of the workspace.

to see that $\Delta\tilde{l}/c$ has the most significant bearing on the tilt angular error ε_θ. This is followed by $\Delta\alpha_2$ and $\Delta\alpha_{03}$. They thereby should strictly be restrained *via* manufacturing and assembly processes. Hence, assign $\Delta\tilde{l}/c$ as the reference level $\Delta p_{\varepsilon,\text{ref}}$, set $\sigma^L_{\varepsilon,\text{ref}} = 0.02/100$ and $3\sigma^U_\theta = 0.1/100$ by considering the ratio of $|\boldsymbol{G}_{\delta\delta}\Delta\boldsymbol{p}_\delta|$ to $|\boldsymbol{G}_{\delta\varepsilon}\Delta\boldsymbol{p}_\varepsilon|$ as well as the manufacturing feasibilities. Meanwhile, assume that all tolerances have equal manufacturing cost, i.e. $w_k = 1/6$. Solving Eq.(12) results in a set of optimized tolerances as shown in Table 2, which are in turn employed as the quality check points over the manufacturing and assembly processes. In order to consolidate the effectiveness of the tolerance design, a LEICA AT901-LR laser tracker with the maximum observed deviation of 0.005mm is used (also see Fig. 4) to measure the coordinates of two points (P_1 and P_2, the center of sphere reflector) on the end-effector. allowing the tilt angular error ε_θ to be evaluated at a given position. In the experiment, the metrology frame $\{O_m\}$ is set at the home position, i.e. the workspace centre P_0 as shown in Fig.3(b), where ε_θ is assumed to be zero. Let point P on subpart 3 undergo eight evenly spaced positions on each circle of radii from 100 mm to 500 mm with an increment of 100 mm while keeping $\phi = 0$. It is observed that ε_θ takes the maximum value of 0.086/100 at the workspace boundary the bottom layer, satisfying the prescribed pose accuracy. Figure 6 shows the distribution of ε_θ across the bottom layer of the workspace, which is obtained by curve fitting to the tilt angles at points evenly spaced in a polar coordinate system. It is easy to see that in the layer ε_θ increases with the increase in radius, and takes the maximum value at workspace boundary.

Table 2 The optimized tolerance allocations (10^{-3} rad)

$T(\Delta\tilde{l}/c)$	$T(\Delta\tilde{c}/c)$	$T(\Delta\alpha_{03})$	$T(\Delta\beta_{03})$	$T(\Delta\alpha_2)$	$T(\Delta\beta_2)$
±0.22	±0.90	±0.26	±0.52	±0.25	±0.84

5.2 Verification of kinematic calibration

Kinematic calibration of the robot is then implemented by two steps. Having built the experiment set-up shown in Fig. 4, the procedures for the rough (encoder offset) and fine calibrations are addressed in what follows.

5.2.1 Rough (encoder offset) calibration

In the rough calibration, let point P on subpart 3 undergo n evenly spaced positions along the boundary of middle layer of the workspace apart from the home position while keeping $\phi \equiv 0$ unchanged at all positions. Given a threshold $\varepsilon_0 = 1\%$, it is easy to see from Fig.7 that the optimal number of the measurement poses is $n = 6$. Therefore, evaluated in $\{O_m\}$ already established in Section 5.1, the realistic coordinates of P at the above positions are measured, resulting in $K = C^2_{6+1} = 21$ distance errors generated by the coordinate measurements. Consequently, the encoder offsets $\Delta\boldsymbol{p}_\theta$ can roughly be identified by using Eq.(21) and the pose error caused by the estimated $\Delta\hat{\boldsymbol{p}}_\theta$ can roughly be compensated using Eq.(22).

In the experiment, the calibration procedure are run twice due to the relatively large encoder offsets until they converge to $\Delta\hat{\theta}_1 = 0.189''$, $\Delta\hat{\theta}_2 = 0.862''$, $\Delta\hat{\theta}_3 = 0.912''$ and $\Delta\hat{\theta}_4 = 0.344''$. It can be seen from Table 3 that the maximum distance, volumetric and rotational error denoted by $\Delta\rho$, Δv and $\Delta\phi$ of

the P_k ($k=1,2,\ldots,6$) relative to P_0 can dramatically be reduced from 2.332mm, 3.816mm and 8.5° to 0.068mm, 0.213 mm and 1.2°, respectively, *via* the rough calibration. Consequently, the encoder offsets become sufficiently small for the use of Eq.(23) that is valid under the first order approximation.

5.2.2 Fine calibration

In the fine calibration, the pose error $\boldsymbol{\delta}$ is to be compensated using full set of source errors being identified. By keeping the home position unchanged, let point *P* undergo n evenly spaced poses along the boundary of top and bottom layers of the workspace. Meanwhile, let the nominal rotational angle ϕ_0 of subpart 3 keeps a constant value of π in the top layer and $-\pi$ in the bottom layer. It is worthwhile pointing out that this arrangement allows the reflector to be adjusted only twice during the entire process for the avoidance of laser beam interference, thereby ensuring the measurement efficiency. Given $\varepsilon_0=1\%$ again, it can be seen from Fig.8 that the optimal number of the measurement poses is $n=9$ for fine calibration. Therefore, nine evenly spaced positions of P apart from P_0 are arranged along a circle of $R_m=500$ mm within each of two layers at $h_m/2=\pm 125$ mm as shown in Fig.3(b). Evaluated in the metrology frame $\{O_m\}$ established by the laser tracker, the realistic coordinates of P at the above positions are measured while keeping subpart 3 a constant rotational angle of $\phi_0=\pm\pi$, equivalently in each layer, resulting in $K=C_{19}^2=171$ distance errors generated by the coordinate measurements.

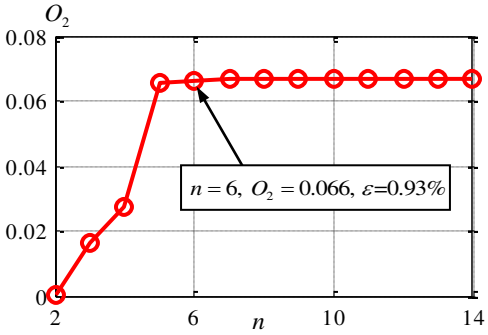

Fig.7 The variations of O_2 *vs.* n in the rough calibration

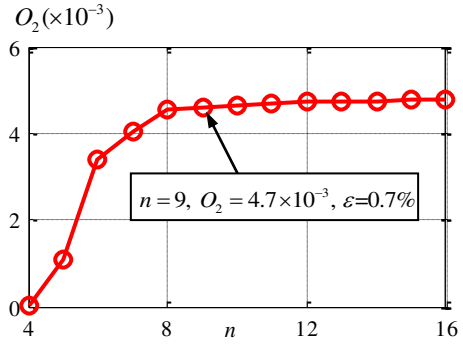

Fig.8 The variations of O_2 *vs.* n in the fine calibration

Table 3 Distance, volumetric and rotational errors before and after encoder offset compensation

Points		P_1	P_2	P_3	P_4	P_5	P_6
Before	$\Delta\rho$	-1.251	-1.361	-1.516	-2.332	-2.082	-1.098
	Δv	3.816	2.994	1.771	3.256	2.568	2.440
	$\Delta\phi$	-0.6	8.5	1.9	-0.2	-2.8	-8.1
After	$\Delta\rho$	-0.017	0.021	0.068	0.025	0.047	0.022
	Δv	0.106	0.096	0.213	0.048	0.086	0.170
	$\Delta\phi$	-0.3	-0.6	-0.4	1.2	0.7	-0.5

Unit: $\Delta\rho$ (mm), Δv (mm) and $\Delta\phi$ (deg).

In the experiment, the calibration procedure needs to be run only once for identifying $\Delta\boldsymbol{p}_\delta$ because sufficient pose accuracy has been achieved thanks to the encoder offset calibration ahead. Each measurement is repeated three times and the mean value is retained. As a result, $\Delta\boldsymbol{p}_\delta$ are identified as represented in Table 4. It should be noted that the estimated values in $\Delta\boldsymbol{p}_\delta$ are not the strictly real source errors because of the existence of the 'measurement errors' arising from $\Delta\boldsymbol{p}_\varepsilon$. Nevertheless, $\boldsymbol{\delta}$ can still be compensated by Eq.(23) using the estimated $\Delta\hat{\boldsymbol{p}}_\delta$ by Eq.(19).

Table 4 Results of source error identification (unit: mm)

	$L\Delta\hat{\theta}_i$	$\Delta\hat{e}_{x,i}$	$\Delta\hat{e}_{y,i}$	$\Delta\hat{e}_{z,i}$	$\Delta\hat{L}_i$	$L\Delta\hat{\alpha}_{0,i}$	$L\Delta\hat{\beta}_{0,i}$	$\Delta\hat{\bar{l}}_i$
Limb 1	-0.347	-0.375	-0.128	-0.707	0.148	0.370	-0.218	-0.577
Limb 2	0.662	--	0.292	---	0.144	0.436	0.049	0.171
Limb 3	0.169	-0.290	-0.258	---	-0.039	-0.372	-0.136	-0.094
Limb 4	-0.187	---	---	---	0.177	-0.433	-0.415	0.511

To evaluate robot accuracy after calibration, eight coordinate measurements on each circle of radii from 100mm to 500 mm with an increment of 100 mm in the top, middle and bottom layers are taken. This makes a total of 120 poses besides the home position. Each validation measurement is repeated three times, and the mean values are retained with the maximum distance standard deviation of 0.006 mm. Acquired using the laser tracker and a rotary encoder mounted on the top of subpart 3, Table 5 shows the maximum distance, volumetric and rotational errors of the end-effector before and after fine calibration. Figure 9 shows the error distributions across the corresponding layer of the workspace as a result of fine calibration. Here, the layer is the one in which the maximum value of the relevant error occurs. It can be seen that the

distribution of the absolute distance error is plane symmetric, it takes quite small values cross the x axis, but eventually increases with the increase of the absolute coordinate of the y axis with the maximum value occurring at the boundary of the bottom layer. The volumetric error eventually increases with the increase of radius and takes the maximum value at the boundary of the bottom layer . Similar to the distribution of the absolute distance error, the distribution of the rotational error of the end-effector relative to subpart 3 is plane symmetric, it takes quite small values cross the y axis, but eventually increases with the increase of the absolute coordinate of the x axis with the maximum value occurring at the boundary of the top layer. The absolute values of these errors are reduced from 0.386 mm to 0.126 mm, from 1.512 mm to 0.472 mm, and from 3.8° to 0.8° over the workspace after the fine calibration.

Table 5 Pose errors before and after fine calibration

	Before	After
$\lvert\Delta\rho\rvert(\mathrm{mm})$	0.386	0.126
$\Delta v(\mathrm{mm})$	1.512	0.472
$\lvert\Delta\phi\rvert(\mathrm{deg})$	3.8	0.8

6. Conclusions

A comprehensive methodology is proposed that incorporates tolerance design with kinematic calibration to ensure the positioning and rotational accuracy of the end-effector of a 4-DOF high-speed parallel robot with articulated travelling plate. The conclusions are drawn as follows:

(1) As an illustration, the uncompensatable tilt angular error of subpart 3 can be restrained below 0.086/100 *via* tolerance design and assembly. This enables kinematic calibration to be carried out using a simplified model and distance measurements, leading to the maximum distance error, volumetric error and rotational error about the z axis of the end-effector relative to subpart 3 are reduced from 0.386mm to 0.126mm, from 1.512 mm to 0.472 mm and from 3.8° to 0.8° over the workspace before and after fine calibration.

(2) Some assumptions have been made on statistic characteristics of the source errors and the cost-tolerance relationship. Therefore, numerous experiments and replications on a batch of machines are expected for further consolidation though the proposed methodology has been tested on a well-engineered prototype.

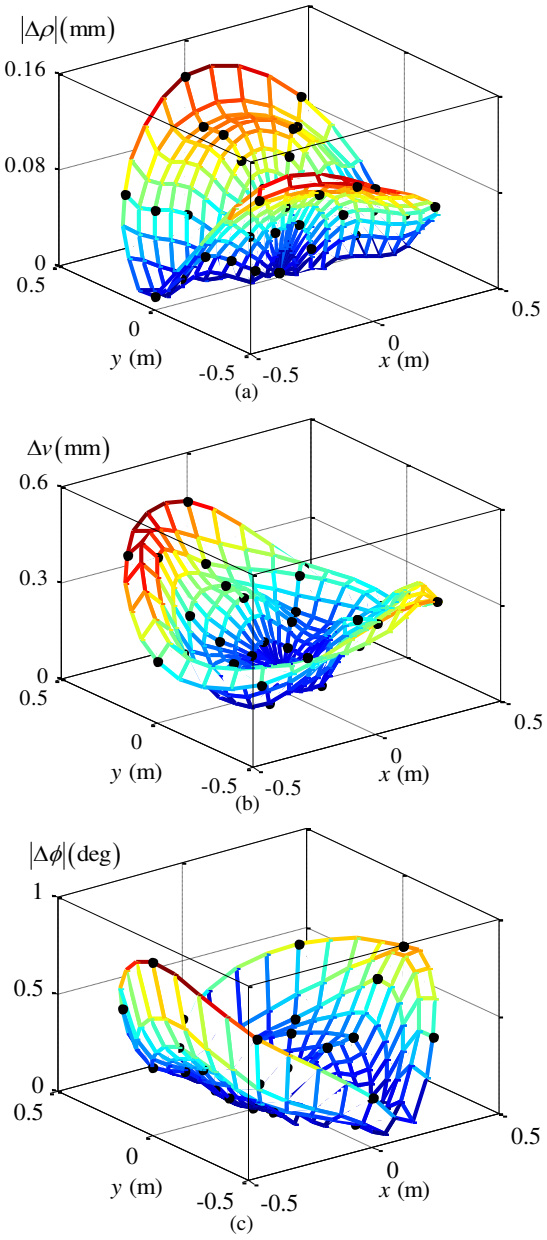

Fig.9 Pose error distributions across the corresponding layer of the workspace after fine calibration, (a) the absolute distance error in the bottom layer, (b) The volumetric error in the bottom layer , (c) the absolute rotational error about the z axis in the top layer.

Acknowledgements

This research work is partially supported by the National Natural Science Foundation of China (NSFC) under Grant 51135008.

References

[1] Pierrot, F., Nabat, V., Company, O., Krut, S., Poignet, P., 2009, "Optimal Design of a 4-DOF Parallel Manipulator: from Academia to Industry," IEEE Trans. Robot., **25**(2), pp. 213-224.

[2] Li, Y. H., Ma, Y., Liu, S. T., Luo, Z. J., Mei, J. P., Huang, T., Chetwynd, D. G., 2014, "Integrated Design of a 4-DOF High-speed Pick-and-place Parallel Robot," Ann. CIRP, **63**(1), pp. 185-188.

[3] Merlet, J. P., 2006, *Parallel Robots*, 2nd ed., Vol. 128 of *Solid Mechanics and Its Applications*, Springer, Netherlands.

[4] Renaud, P., Andreff, N., Martinet, P., Gogu, G., 2005, "Kinematic Calibration of Parallel Mechanisms: a Novel Approach using Legs Observation," IEEE Trans. Robot., **21**(4), pp. 529-538.

[5] Jeon, D., Kim, K., Jeong, J. I., Kim, J., 2010, "A Calibration Method of Redundantly Actuated Parallel Mechanism Machines Based on Projection Technique," Ann. CIRP, **59**(1), pp. 413-416.

[6] Takeda, Y., Shen, G., Funabashi, H., 2004, "A DBB-Based Kinematic Calibration Method for In-parallel Actuated Mechanisms using a Fourier Series," ASME J. Mech. Des., **126**(1), pp. 856-865.

[7] Corbel, D., Nabat, V., Maurine, P., 2006, "Geometrical Calibration of the High Speed Robot Par4 using a Laser Tracker," *Proceedings of the 12th IEEE International Conference on Methods and Models in Automation and Robotics (MMAR)*, Miedzyzdroje, Poland, pp. 687-692.

[8] Deblaise, D., Maurine, P., 2005, "Effective Geometrical Calibration of a Delta Parallel Robot Used in Neurosurgery," *Proceedings of the IEEE/RSJ International Conference on*

Intelligent Robots and Systems (IROS 2005), Alberta, Canada, pp. 1313-1318.

[9] Vischer, P., Clavel, R., 1998, "Kinematic Calibration of the Parallel Delta Robot," Robotica, **16**(2), pp. 207-218.

[10] Huang, T., Whitehouse, D. J., Chetwynd, D. G., 2002, "A Unified Error Model for Tolerance Design, Assembly and Error Compensation of 3-DOF Parallel Kinematic Machines with Parallelogram Struts," Ann. CIRP, **51**(1), pp. 297–301.

[11] Bai, P., Mei, J., Huang, T., Chetwynd, D. G., 2016, "Kinematic Calibration of Delta Robot Using Distance Measurements," P. I. Mech. Eng. C-J. Mec., **230**(3), pp. 414-424.

[12] Caro, S., Wenger, P., Bennis, F., Chablat, D., 2006, "Sensitivity Analysis of the Orthoglide, A 3-DOF Translational Parallel Kinematic Machine," ASME J. Mech. Des., **128**(1), pp. 392–402.

[13] Briot, S., Bonev, I. A., 2010, "Accuracy Analysis of 3T1R Fully-Parallel Robots, " Mech. Mach. Theory, **45**(5), pp. 695-706.

[14] Huang, T., Chetwynd, D. G., Mei, J. P., Zhao, X. M., 2006, "Tolerance Design of a 2-DOF Overconstrained Translational Parallel Robot," IEEE Trans. Robot., **22**(1), pp. 167-172.

[15] Schellekens, P., Rosielle, N., Vermeulen, H., Vermeulen, M., Wetzels, S., Pril, W., 1998, "Design for Precision: Current Status and Trends," Ann. CIRP, **47**(2), pp. 557-586.

[16] Prabhaharan, G., Asokan, P., Ramesh, P., Rajendran, S., 2004, "Genetic-algorithm-based Optimal Tolerance Allocation using a Least-cost Model," J. Adv. Manufact. Technol., **24**(9), pp. 647-660.

[17] Caro, S., Bennis, F., Wenger, P., 2005, "Tolerance Synthesis of Mechanisms: a Robust Design Approach," ASME J. Mech. Des., **127**(1), pp. 86-94.

[18] Dumas, A., Gayton, N., Dantan, J. Y., Sudret, B., 2015, "A New System Formulation for the Tolerance Analysis of Overconstrained Mechanisms," Probabilist. Eng. Mech., **40**(1), pp. 66-74.

[19] Goldsztejn, A., Caro, S., Chabert, G., 2015, "A New Methodology for Tolerance Synthesis of Parallel Manipulators," *Proceedings of the 14th World Congress in Mechanism and Machine Science*, Taipei, Taiwan, pp.132-141.

[20] Wu, Y., Klimchik, A., Caro, S., Furet, B., Pashkevich, A., 2015, "Geometric Calibration of Industrial Robots Using Enhanced Partial Pose Measurements and Design of Experiments," Robot. Cim-Int. Manuf., **35**(1), pp. 151 – 168.

[21] Borm, J. H., Menq, C. H., 1991, "Determination of Optimal Measurement Configurations for Robot Calibration Based on Observability Measure," Int. J. Robot. Res., **10**(1), pp. 51-63.

[22] Driels, M. R., Pathre, U. S., 1990, "Significance of Observation Strategy on the Design of Robot Calibration Experiments," J. Robotic Syst., **7**(2), pp. 197-223.

[23] Khalil, W., Gautier, M., Enguehard, Ch., 1991, "Identifiable Parameters and Optimum Configurations for Robots Calibration," Robotica, **9**(1), pp. 63–70.

[24] Chase, K. W., Greenwood, W. H., Loosli, B. G., Hauglund, L. F., 1990, "Least Cost Tolerance Allocation for Mechanical Assemblies with Automated Process Selection," Manufacturing Review, **3**(1), pp. 49-59.

[25] Huang, T., Chetwynd, D. G., Whitehouse, D. J., Wang, J., 2005, "A General and Novel Approach for Parameter Identification of 6-DOF Parallel Kinematic Machines," Mech. Mach. Theory, **40**(2), pp. 219-239.

[26] Daney, D., Madeline, B., Papegay, Y., 2005, "Choosing Measurement Poses for Robot Calibration with Local Convergence Method and Tabu Search," Int. J. Robot. Res., **24**(6), pp. 501-518.

[27] Sun, Y., Hollerbach, J. M., 2008, "Observability Index Selection for Robot Calibration," *Proceedings of the IEEE International Conference on Robotics and Automation (ICRA 2008)*, Pasadena, CA, USA, pp. 831-836.

[28] Joubair, A., Bonev, I. A., 2013, "Comparison of the Efficiency of Five Observability Indices for Robot Calibration," Mech. Mach. Theory, **70**(6), pp. 254–265.

[29] Joubair, A., Nubiola, A., Bonev, I., 2013, "Calibration Efficiency Analysis Based on Five Observability Indices and Two Calibration Models for a Six-Axis Industrial Robot," SAE Int. J. Aerospace, **6**(1) , pp. 161-168.

[30] ISO 9283, 1998, "Manipulating Industrial Robots - Performance Criteria and Related Test Methods," International Standards Organization, pp. 21-22.